

Microstructural Evolution and Deformation Behavior of Ni-Si- and Co-Si-Containing Metastable High Entropy Alloys



S. SINHA, S.S. NENE, M. FRANK, K. LIU, R.S. MISHRA, B.A. MCWILLIAMS, and K.C. CHO

Two high entropy alloy (HEA) compositions were compared to explore the individual effects of Co and Ni on phase stability and resultant deformation response in Fe-Mn-Cr-Si-containing HEAs. It was observed that Co-Si-containing HEA depicted responsive phase evolution upon friction stir processing owing to decreased γ (f.c.c.) matrix stability as against Ni-Si-containing HEA. As a result, the Co-Si HEA showed the presence of dual-phase microstructure with the dominance of ε (h.c.p.) phase (52 pct), whereas the Ni-Si HEA showed single-phase γ microstructure under similar processing condition. Also, the dominant deformation mechanisms were different in the two alloys. Co-Si HEA showed uniform strain partitioning between the f.c.c. and h.c.p. phases. Conversely, single-phase f.c.c. microstructure in Ni-Si HEA accommodated strain by twinning-induced plasticity.

<https://doi.org/10.1007/s11661-018-4968-6>

© The Minerals, Metals & Materials Society and ASM International 2018

I. INTRODUCTION

THE advent of nonequiatomic high entropy alloys (HEAs) from the traditional approach that focuses on single-phase equiatomic HEAs has created enormous scope for designing compositions with tailored metastability of phases.^[1–6] The fundamental basis in the quest for enhanced mechanical properties in these nonequiatomic HEAs is focused on exploiting the benefits of previously established deformation mechanisms such as transformation-induced plasticity (TRIP) and twinning-induced plasticity.^[1,4–6] Li and Raabe^[3] explained that the activation of multiple deformation mechanisms is a key to the design of nonequiatomic HEAs that exhibit adequate strength and ductility.

The broad objective of the present research effort is to design nonequiatomic HEAs, the microstructure and deformation response of which can be tailored through their chemistry and processing, to incorporate the effect of various mechanisms like phase transformation, twinning, dislocation, and precipitation strengthening, while

maintaining the core effects of HEAs.^[7–9] Friction stir processing (FSP) of these metastable HEAs enables microstructural refinement with some control over temperature, strain, and strain rate.^[10]

Previously, Nene *et al.*^[11,12] discussed FSP-engineered dual-phase HEAs where enhanced strength and ductility were the result of pronounced TRIP in the material. Subsequently, a remarkable strength–ductility combination was achieved,^[13] wherein the effects of transformation and twinning were incorporated successfully. Those previous studies highlighted the advantages that can be obtained by martensitic transformation in terms of strength–ductility tradeoff, generating interest in studying various aspects of the transformation like its dependence on alloy chemistry, fundamental understanding of the ε (h.c.p.) martensite phase in HEAs, and the kinetics of martensite formation. Therefore, it is imperative to be able to control the transformation driving force and kinetics so that h.c.p. phase formation can be promoted or inhibited where necessary. In line with this, the current paper is not about achieving superior mechanical properties by changing the alloy chemistry. Instead, it seeks to explain the selective predominance of strain accommodation mechanisms based on the difference in the phase stability in the newly developed HEAs. This study outlines the dependence of martensitic transformation on alloy chemistry by specifically comparing two friction stir processed HEAs to illustrate the effect of Co or Ni on the γ (f.c.c.) metastability and concurrent mechanical response. The constituent elements in these HEAs make them similar

S. SINHA, S.S. NENE, M. FRANK, K. LIU, and R.S. MISHRA are with the Center for Friction Stir Processing, Department of Materials Science and Engineering, University of North Texas, Denton, TX 76207. Contact e-mail: Rajiv.Mishra@unt.edu B.A. MCWILLIAMS and K.C. CHO are with the Weapons and Materials Research Directorate, U.S. Army Research Laboratory, Aberdeen Proving Grounds, Aberdeen, MD 21005.

Manuscript submitted August 7, 2018.

Article published online October 23, 2018

to austenitic stainless steels and, therefore, can be considered as useful candidates in structural applications.^[14,15]

II. EXPERIMENTAL METHODOLOGY

A. Materials

Two nonequiatomic HEAs with actual compositions (in at. pct) shown in Table I were considered. The Fe-Mn-Ni-Cr-Si-containing HEA is referred to as Ni-Si HEA, while the Fe-Mn-Co-Cr-Si-containing HEA is referred to as Co-Si HEA. The HEAs were produced by vacuum arc-casting in a cold-copper crucible. The vacuum level achieved was approximately 300 μm , and the chamber was backfilled with argon to 1 atm prior to each melt. The HEAs were produced using pure metals and ingot dimensions of 300 \times 100 \times 6 mm³.

B. Friction Stir Processing

Table II presents the parameters for carrying out double-pass (D-pass) FSP [two overlapping FSP runs at 650 rotations per minute (RPM) and 350 RPM]. FSP was carried out on the 6-mm as-cast HEA sheets using tungsten-rhenium (W-Re) tool. The dimensions of the processing tool were 12 mm shoulder diameter with tapered pin, 7.5 mm root diameter, 6 mm pin tip diameter, and 3.5 mm pin length.

C. Tensile Testing

Room-temperature tensile tests to failure were carried out in a mini-tensile tester at an initial strain rate of 10^{-3} s^{-1} . Flat (rectangular) dog-bone-shaped mini-tensile specimens with gage length of 5 mm, width of 1.25 mm, and thickness of 1 mm were machined out using a mini computer numerical control machine from the top surface of the as-cast ingot and from 1 mm below the surface from the stirred region of the friction stir processed material. For each condition, three tests were carried out to confirm the reproducibility of results.

Table I. Actual Compositions (in At. Pct) After Casting of the Two HEAs

| Alloys | Fe | Mn | Co | Ni | Cr | Si |
|-----------|------|------|------|-----|------|-----|
| Ni-Si HEA | 42.8 | 28.3 | — | 9.6 | 14.8 | 4.5 |
| Co-Si HEA | 43.0 | 27.7 | 10.7 | — | 14.0 | 4.6 |

Table II. FSP Parameters Used in the Present Study

| Conditions | Rotational Rate (RPM) | Traverse Speed (mm/min) | Plunge Depth (mm) | Tilt Angle (Deg) |
|------------|-----------------------|-------------------------|-------------------|------------------|
| Pass 1 | 650 | 50.8 | 3.85 | 2 |
| Pass 2 | 350 | 50.8 | 3.85 | 2 |

D. Microstructural Characterization

Microstructures of the as-cast, friction stir processed, and tensile-deformed specimens were characterized using electron backscattered diffraction (EBSD) on a FEI Nova Nano SEM 230 equipped with Hikari Super EBSD detector using an operating voltage of 20 kV. The EBSD scan area for the as-cast material was roughly 350 μm \times 250 μm , and the step size of acquisition was 0.5 μm . The FSP material had significantly finer grain size. Hence, EBSD scans were carried out at higher magnification (2000X), wherein an area of 75 μm \times 60 μm could be captured. The step size for these scans was 0.2 μm . For reliability of results and to include enough number of grains in data analysis, three scans were carried out for each specimen. TEAMTM EBSD analysis system was used for EBSD data acquisition, and TSL OIM Version 8 software was used for data analysis. Fractography of tensile specimens was carried out using a FEI Quanta 200 ESEM.

E. X-Ray Diffraction

X-ray diffraction (XRD) measurements of the as-cast and tensile-deformed specimens of Ni-Si HEA and Co-Si HEA were carried out using Rigaku Ultima III diffractometer and Cu K α radiation operating at 40 kV and 44 mA.

III. RESULTS

A. As-cast and As-FSP Microstructure

Figures 1(a) and (b) are EBSD inverse pole figure (IPF) maps for the as-cast microstructures of the Ni-Si HEA and Co-Si HEA, respectively. The as-cast material consists of aggregate of coarse grains with various IPF normal direction (ND) orientations. Both alloys show coarse-grained γ (f.c.c.) matrix; however, while Ni-Si HEA is single-phase γ (f.c.c.), Co-Si HEA contains 9 pct ϵ (h.c.p.) martensite phase, as observed in the EBSD phase maps (Figures 1(c) and (d)). The ϵ (h.c.p.) martensite phase is distributed throughout the γ (f.c.c.) matrix. Comparison of Figures 1(b) and (d) indicates that most of the ϵ (h.c.p.) phase in the as-cast Co-Si HEA is basal oriented (IPF ND oriented toward $\langle 0001 \rangle$), which is the preferred orientation for nucleation of the ϵ (h.c.p.) martensite. The orientation relationship between ϵ (h.c.p.) martensite and γ (f.c.c.) is illustrated in Figure 1(e) which shows the unit cell orientations in the two phases. It is observed that the $\{0001\}$ basal plane of ϵ (h.c.p.) is oriented with the $\{111\}$ plane of γ (f.c.c.).

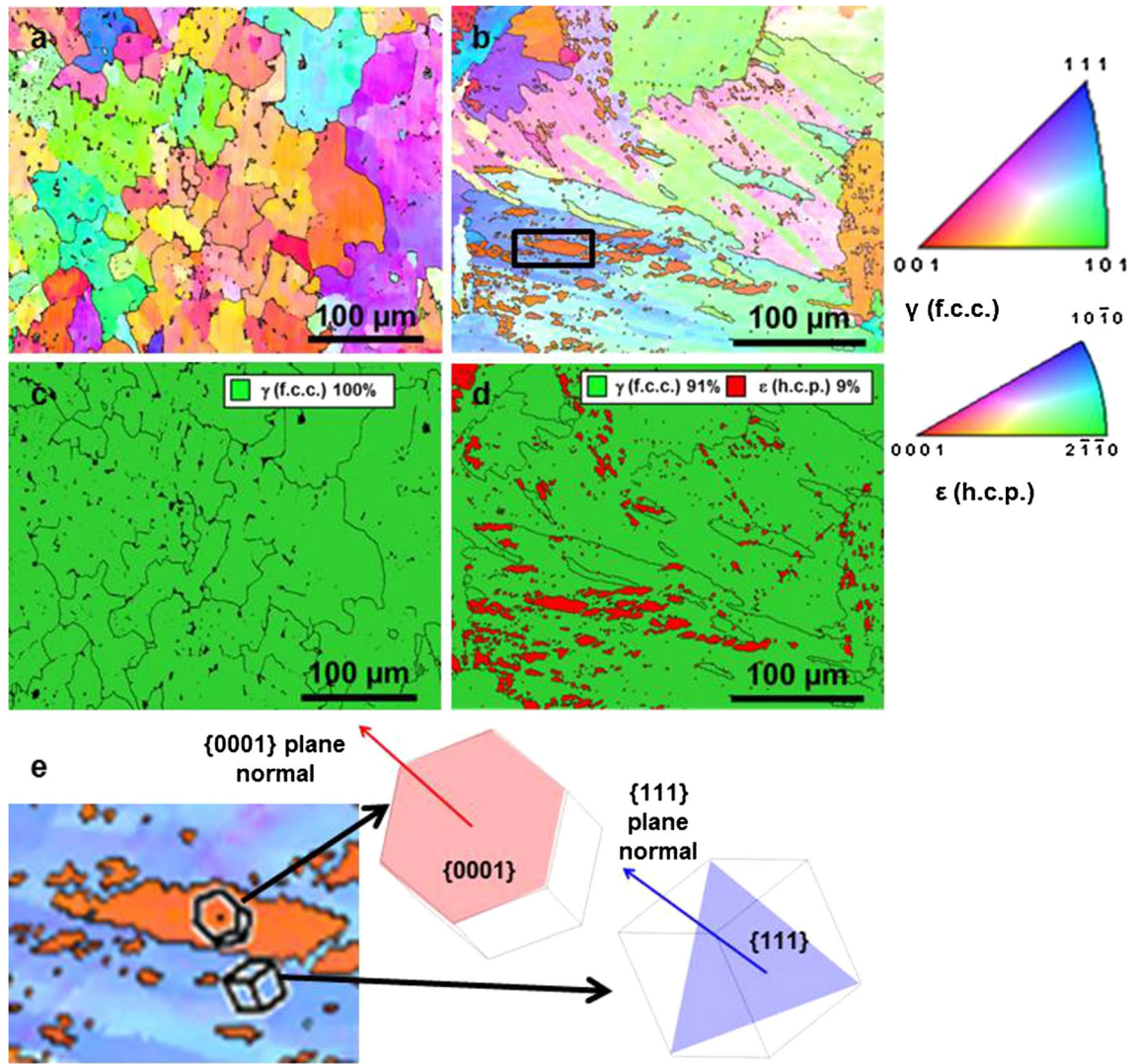


Fig. 1—(a, b) EBSD IPF maps and (c, d) corresponding phase-fraction maps showing the as-cast microstructures for (a, c) Ni-Si HEA and (b, d) Co-Si HEA; (e) enlarged IPF map portion of region marked in black box in (b) with corresponding unit cells showing orientation relationship.

Figures 2(a) and (b) show the EBSD phase map and IPF map, respectively, for the as-processed specimen of Ni-Si HEA. The microstructure consists of single-phase γ (f.c.c.). The phase-fraction map for the as-processed Co-Si HEA specimen is shown in Figure 2(c), while the corresponding IPF map portions for γ (f.c.c.) and ϵ (h.c.p.) grains are shown in Figures 2(d) and (e), respectively. FSP leads to considerably grain-refined microstructure with equiaxed grains in both alloys. However, the Co-Si HEA shows more grain refinement than Ni-Si HEA. The Ni-Si HEA has average grain sizes of $13.7 \mu\text{m}$ in the as-cast condition and $1.8 \mu\text{m}$ in the D-pass FSP condition. In comparison, the grain sizes of Co-Si HEA in the as-cast condition are $15.2 \mu\text{m}$ for γ (f.c.c.) and $3.6 \mu\text{m}$ for ϵ (h.c.p.), while in the as-FSP condition, the average grain sizes of γ (f.c.c.) and ϵ (h.c.p.) phases are 0.8 and $0.5 \mu\text{m}$, respectively. As is also evident from Figure 2(c), unlike Ni-Si HEA, Co-Si HEA displays considerable transformation from γ

(f.c.c.) to ϵ (h.c.p.), and results in a dual-phase microstructure. This responsive microstructural evolution in these materials irrespective of the same processing history is indicative of alloy chemistry-driven phase stability in these HEAs. The as-FSP microstructure of Co-Si HEA contains 52 pct ϵ (h.c.p.) phase, and the ϵ (h.c.p.) grains are mostly oriented with IPF ND near basal $\{0001\}$ direction (Figure 2(e)), similar to that observed in the as-cast material (Figures 1(b) and (d)). The micro-textures obtained for the γ (f.c.c.) and ϵ (h.c.p.) grains also indicate the previously observed orientation relationship between the two phases, as observed from the pole figures in Figures 3(a) and (b). The γ (f.c.c.) phase shows high intensity of 111, while ϵ (h.c.p.) shows 0001 basal texture, and since both phases are evenly distributed in the microstructure (Figures 2(d) and (e)), it can be concluded that the ϵ (h.c.p.) martensite has $\{0001\} // \{111\}$ of γ (f.c.c.) orientation relationship.

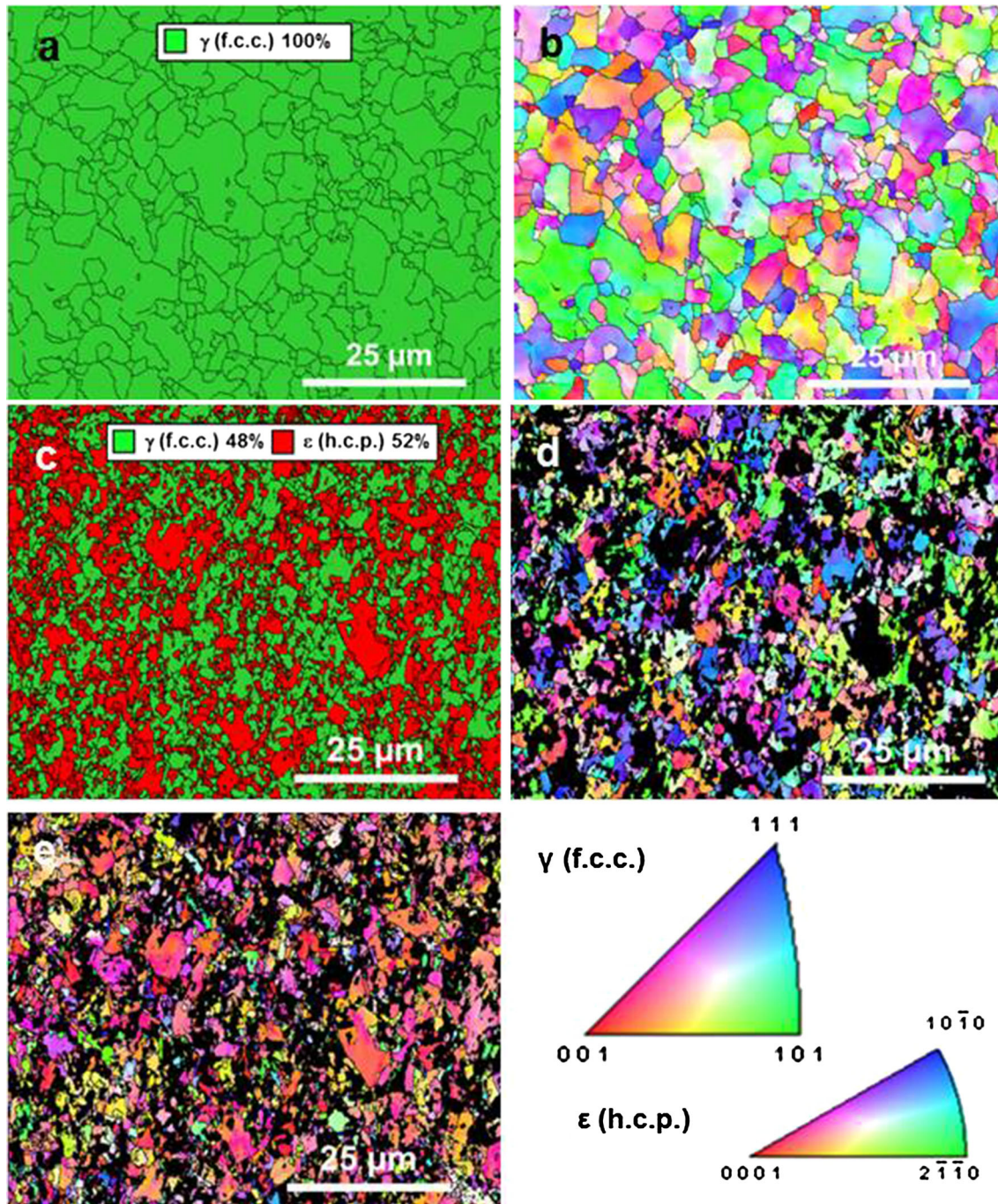


Fig. 2—(a) EBSD phase map and (b) IPF map for Ni-Si HEA D-pass FSP specimen; (c) EBSD phase-fraction map for Co-Si HEA D-pass specimen; IPF maps for (d) γ (f.c.c.) and (e) ϵ (h.c.p.) grains in Co-Si HEA D-pass specimen.

B. Tensile Properties, Strain-Hardening, and Fracture Behavior

Figure 4(a) presents engineering stress–strain curves for the as-cast material and D-pass specimens of Ni-Si HEA and Co-Si HEA. The as-cast Ni-Si HEA exhibits yield strength (YS) of 291 MPa, ultimate tensile strength (UTS) of 396 MPa, and ~ 8 pct elongation; while the as-cast Co-Si HEA has 398 MPa YS, 611 MPa UTS, and 7 pct elongation. Clearly, for both alloys, the FSP materials show significant improvements in strength and

ductility compared with the as-cast materials. However, within the two HEAs, Co-Si HEA exhibits significantly higher strength than Ni-Si HEA, while retaining similar ductility. For Ni-Si HEA, D-pass FSP specimen shows 633 MPa UTS and around 34 pct elongation, while Co-Si HEA D-pass FSP specimen shows almost 900 MPa UTS with about 32 pct elongation. The strain-hardening response plotted in Figure 4(b) also indicates that the Co-Si HEA D-pass specimen shows higher work hardening compared with the Ni-Si HEA

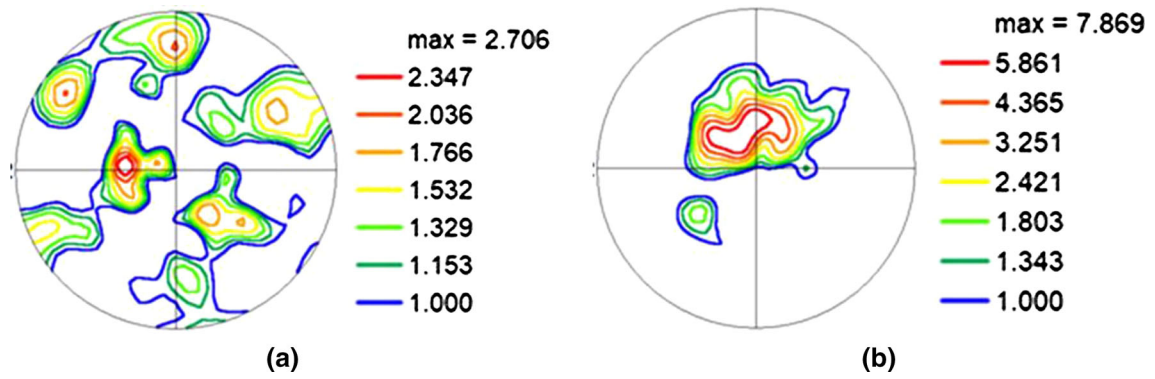


Fig. 3—(a) 111 Pole figure for γ (f.c.c.) grains shown in Fig. 2(d); (b) 0001 pole figure for ϵ (h.c.p.) grains shown in Fig. 2(e) for Co-Si HEA D-pass specimen.

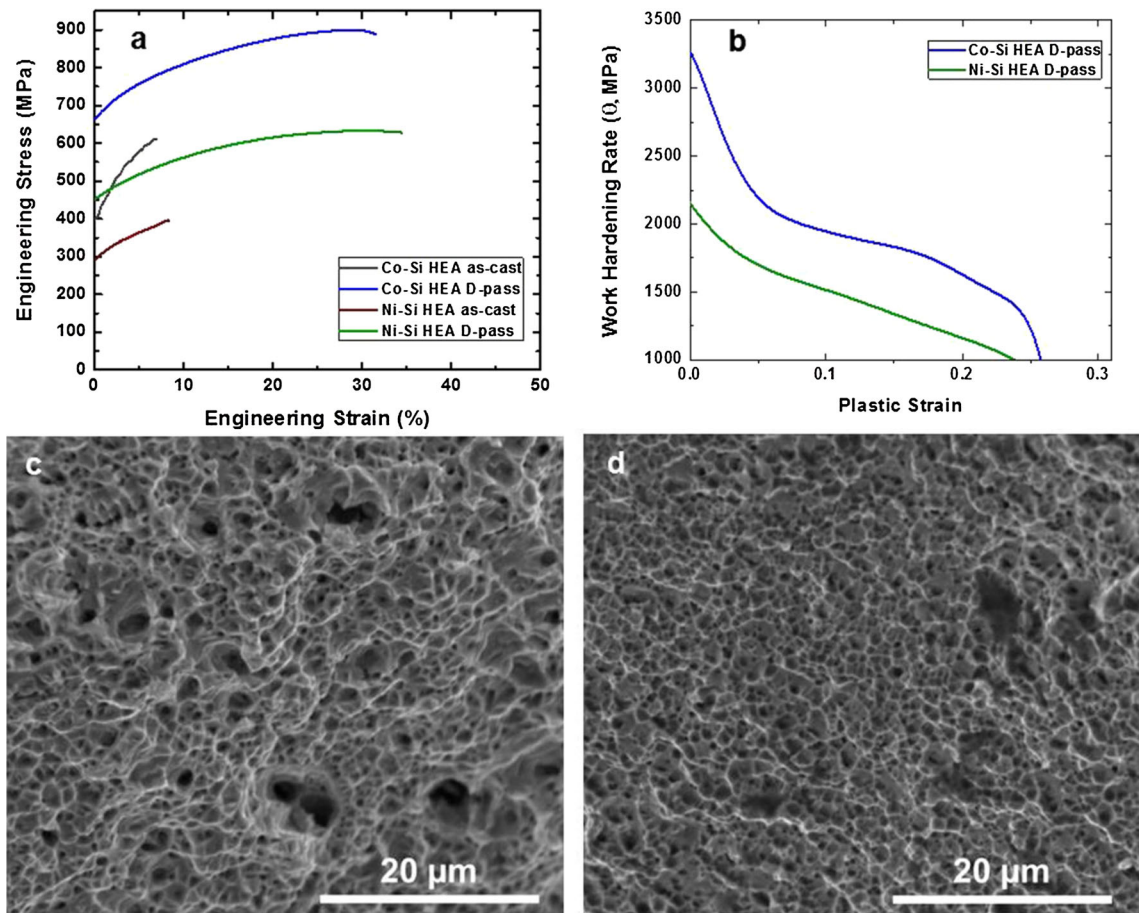


Fig. 4—(a) Engineering stress–strain curves for the as-cast and D-pass specimens and (b) strain-hardening curves for D-pass specimens of Ni-Si HEA and Co-Si HEA. Fracture surfaces of D-pass tensile specimens for (c) Ni-Si HEA and (d) Co-Si HEA.

D-pass specimen. Therefore, clearly, Co-Si HEA exhibits better tensile properties than Ni-Si HEA. The difference in mechanical response between the two alloys suggests that the microstructure-dependent operative deformation mechanisms are different in the two alloys.

Fractography of tensile specimens was carried out to examine the failure characteristics of these materials. Figures 4(c) and (d) show the fracture surfaces of tensile specimens of Ni-Si HEA and Co-Si HEA D-pass

specimens, respectively. Although both specimens depict typical dimpled rupture characteristics of ductile failure, the Co-Si HEA specimen exhibits much finer dimples, while the dimples in Ni-Si HEA are visibly coarser. In addition, the fracture surface of the Ni-Si HEA specimen contains still deeper voids. These fractography features confirm that Ni-Si HEA is characterized by a higher tendency toward larger cavity-driven failure compared with Co-Si HEA.

C. Microstructural Evolution During Tensile Deformation

EBSD IPF maps in Figures 5(a) and (b) present the microstructures after tensile deformation of the as-cast specimens of Ni-Si HEA and Co-Si HEA, respectively. The coarse-grained microstructures in the as-cast specimens limit the tensile performance of the as-cast material. In addition, phase-fraction maps for the tensile-deformed as-cast specimens of Ni-Si HEA and Co-Si HEA (Figures 5(c) and (d), respectively) clearly illustrate the contrast between the two alloys. Ni-Si HEA shows single-phase γ (f.c.c.), while Co-Si HEA shows ϵ (h.c.p.)-dominated dual-phase microstructure, highlighting the metastability of the γ (f.c.c.) phase in the latter alloy that triggered transformation during deformation.

Figures 6(a) through (d) show the microstructures of tensile-deformed specimens of D-pass Ni-Si HEA and Co-Si HEA. The EBSD image quality (IQ) maps denote more grain-refined microstructure with higher dislocation density in Co-Si HEA (Figure 6(b)) than Ni-Si HEA (Figure 6(a)). This indicates that Co-Si HEA accommodates higher amount of dislocation content than Ni-Si HEA for the same amount of strain, which accounts for the higher strength and work hardening obtained for this alloy. The phase-fraction maps in Figures 6(c) and (d) illustrate that while there is no transformation from γ (f.c.c.) to ϵ (h.c.p.) in Ni-Si HEA, ϵ (h.c.p.) fraction in the Co-Si HEA D-pass specimen

increases from 52 pct in the as-FSP condition (Figure 2(c)) to 65 pct after tensile deformation.

The microstructural dependence of the mechanical response in the as-cast material also clearly indicated that improvement in strength is associated with ϵ (h.c.p.) martensitic microstructure although limited ductility is obtained. In contrast, the FSP material showed improvement in strength and ductility in both alloys. Therefore, it is clear that while the effect of strain, strain rate, and temperature during FSP is integral to obtaining better mechanical properties, tailoring the microstructure to achieve controlled transformation is dependent on the alloy chemistry-driven phase stability inherent in the alloys. The inherent dependence of martensitic transformation on the phase stability is also proven by the fact that the as-cast Co-Si HEA material showed higher amount of transformation after tensile deformation (9 pct h.c.p. in Figure 1(d) to 89 pct h.c.p. in Figure 5(d)) compared with the as-FSP material (52 pct h.c.p. in Figure 2(c) to 65 pct h.c.p. in Figure 6(d)). On the other hand, Ni-Si HEA with the increased γ (f.c.c.) stability showed no transformation in the as-cast material (100 pct f.c.c. in Figures 1(c) and 5(c)) or the FSP material (100 pct f.c.c. in Figures 2(a) and 6(c)). The essence of invoking controlled transformation was captured by exploring the dependence of strain accommodation mechanisms on untransformed and transformed microstructures. This was established by analyzing the dislocation evolution and local misorientation in the microstructure of these alloys.

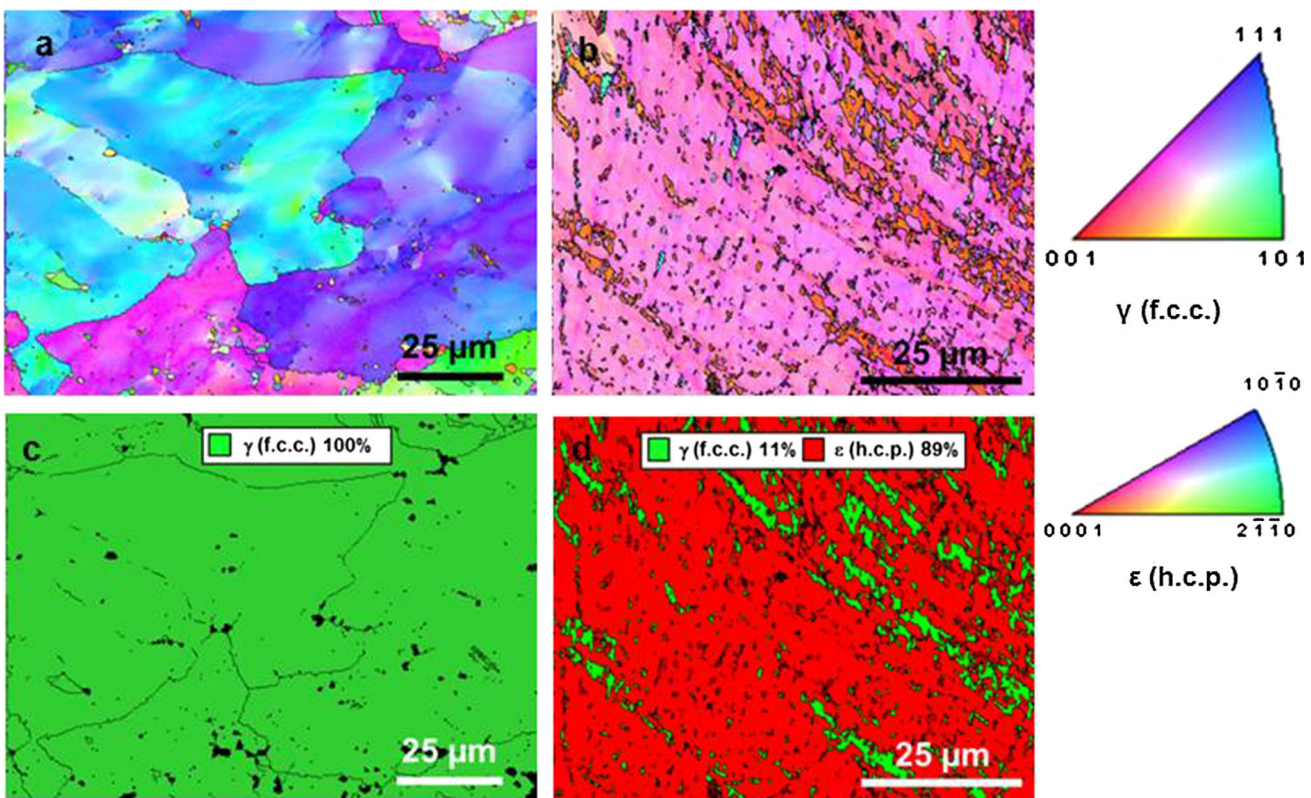


Fig. 5—EBSD IPF maps (a, b) and corresponding phase-fraction maps (c, d) showing tensile-deformed microstructure of the as-cast material for (a, c) Ni-Si HEA and (b, d) Co-Si HEA.

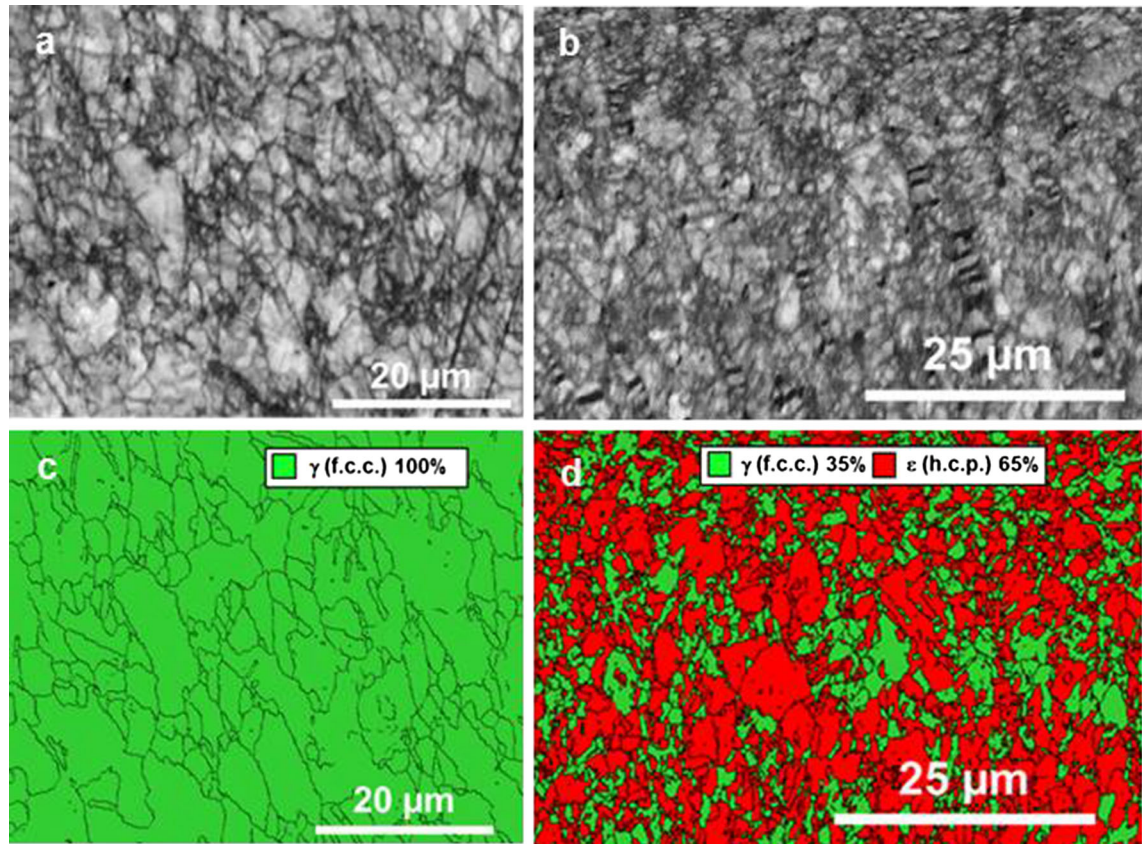


Fig. 6—Microstructures after tensile deformation for D-pass specimens of Ni-Si HEA (*a, c*) and Co-Si HEA (*b, d*); [corresponding image quality (IQ) maps and phase-fraction maps in (*a*) and (*c*) for Ni-Si HEA and in (*b*) and (*d*) for Co-Si HEA].

Table III. GND Densities in γ (f.c.c.) and ϵ (h.c.p.) Phases in Ni-Si HEA and Co-Si HEA Specimens in Comparison Under Various Conditions

| Alloys | Specimen | f.c.c. $1/2\langle 110 \rangle$ ($\times 10^{12} \text{ m}^{-2}$) | h.c.p. $\langle c + a \rangle$ ($\times 10^{12} \text{ m}^{-2}$) |
|-----------|------------------|---|--|
| Ni-Si HEA | As-cast | 459 | — |
| | As-cast Deformed | 627 | — |
| | D-Pass FSP | 994 | — |
| | D-Pass Deformed | 1522 | — |
| Co-Si HEA | As-cast | 245 | 814 |
| | As-cast Deformed | 778 | 1110 |
| | D-Pass FSP | 2546 | 4576 |
| | D-Pass Deformed | 2646 | 3994 |

The evolution of geometrically necessary dislocation (GND) density was evaluated for the various specimens of Ni-Si HEA and Co-Si HEA. GND densities were calculated using TSL-OIM software, the procedure for which is described in Reference 16. Table III shows GND densities in γ (f.c.c.) and ϵ (h.c.p.) phases in various conditions of Ni-Si HEA and Co-Si HEA. Ni-Si HEA [single-phase γ (f.c.c.)] shows lower overall GND density ($\sim 1.5 \times 10^{15} \text{ m}^{-2}$ in the D-pass-deformed condition) than Co-Si HEA. In the case of Co-Si HEA, D-pass-deformed condition has higher γ (f.c.c.) GND density as well as significant $\langle c + a \rangle$ dislocation density values in the ϵ (h.c.p.) phase [$\sim 2.6 \times 10^{15} \text{ m}^{-2}$ in γ

(f.c.c.) and $\sim 4 \times 10^{15} \text{ m}^{-2} \langle c + a \rangle$ in ϵ (h.c.p.)]. The higher GND content accommodated by the dual-phase microstructure accounts for the higher stress accommodated at similar level of strain and higher work hardening in Co-Si HEA than Ni-Si HEA.

Kernel average misorientation (KAM) maps with corresponding IPF map portions are shown for γ (f.c.c.) phase in Ni-Si HEA (Figures 7(a) and (b)) and Co-Si HEA (Figures 7(c) and (d)) and for ϵ (h.c.p.) phase in Co-Si HEA (Figures 7(e) and (f)). The KAM map for Ni-Si HEA reveals several coarse grains in this material, which show low KAM (for example, those circled in black in the IPF map in Figure 7(a)), while most of the

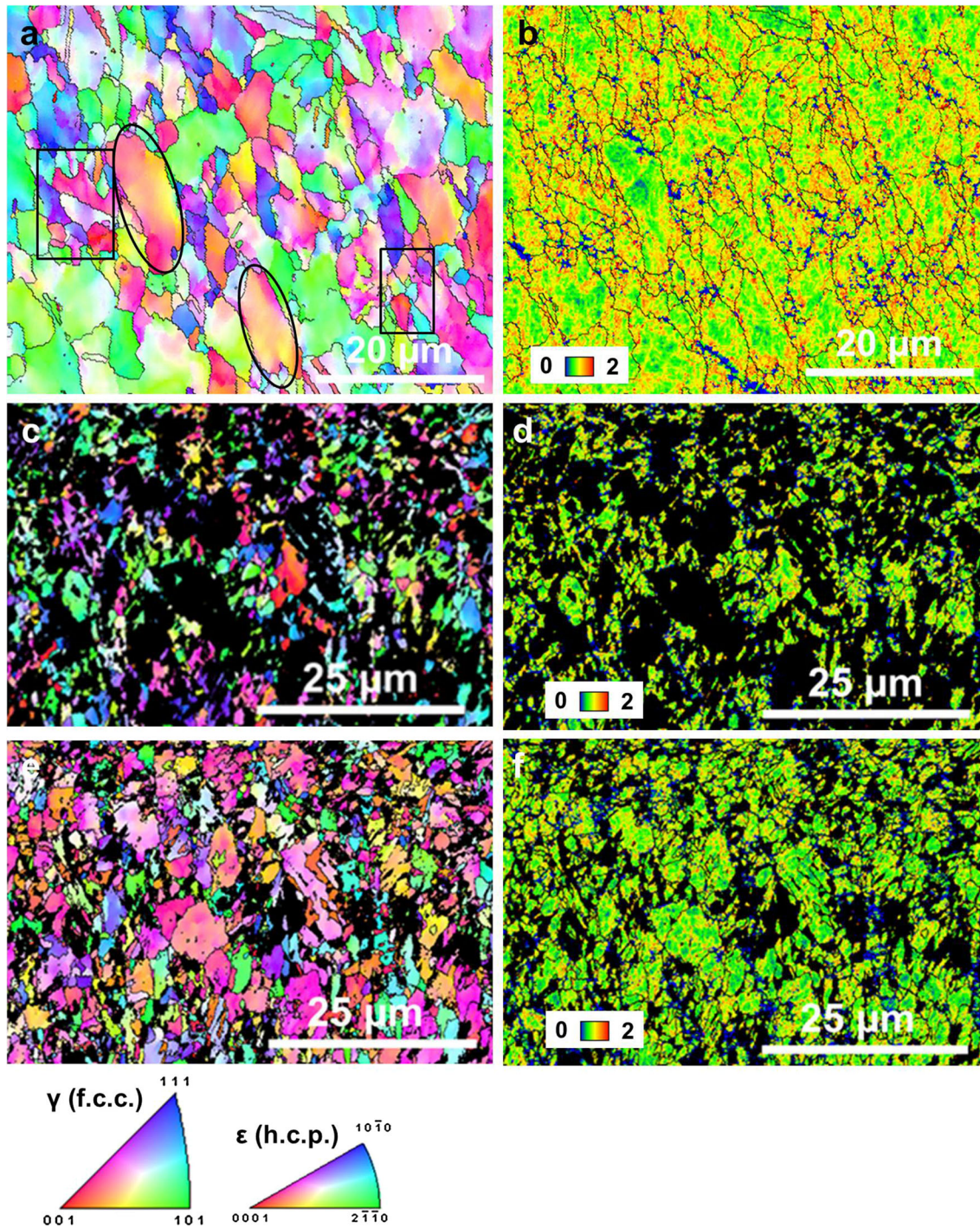


Fig. 7—Corresponding IPF maps (*a, c, e*) and kernel average misorientation (KAM) maps (*b, d, f*) for D-pass-deformed specimens of (*a, b*) γ (f.c.c.) phase in Ni-Si HEA (*c, d*) γ (f.c.c.) phase in Co-Si HEA (*e, f*) ϵ (h.c.p.) phase in Co-Si HEA.

strain is accommodated by the surrounding finer grains, which show higher KAM (outlined by black boxes in Figure 7(a)). In contrast, the KAM maps for γ (f.c.c.) and ϵ (h.c.p.) grains (Figures 7(d) and (f) respectively) in Co-Si HEA show higher KAM and indicate that strain is equally partitioned between the two phases in D-pass-deformed Co-Si HEA specimen.

Figure 7(b) shows relatively lower KAM in the coarse grains in Ni-Si HEA than that in the finer grains.

However, bigger grains being favorable for twin nucleation,^[17,18] a few of these larger grains exhibit twinning (IPF map portions in Figure 8(a)). The misorientation angle chart in Figure 8(b) [shown for one of the twins marked in Figure 8(a)] illustrates the occurrence of 60 deg- $\langle 111 \rangle$ f.c.c. twins that are about 1.5 μm thick. Thus, absent any transformation, the available strain accommodating mechanism in Ni-Si HEA is through f.c.c. twin formation.

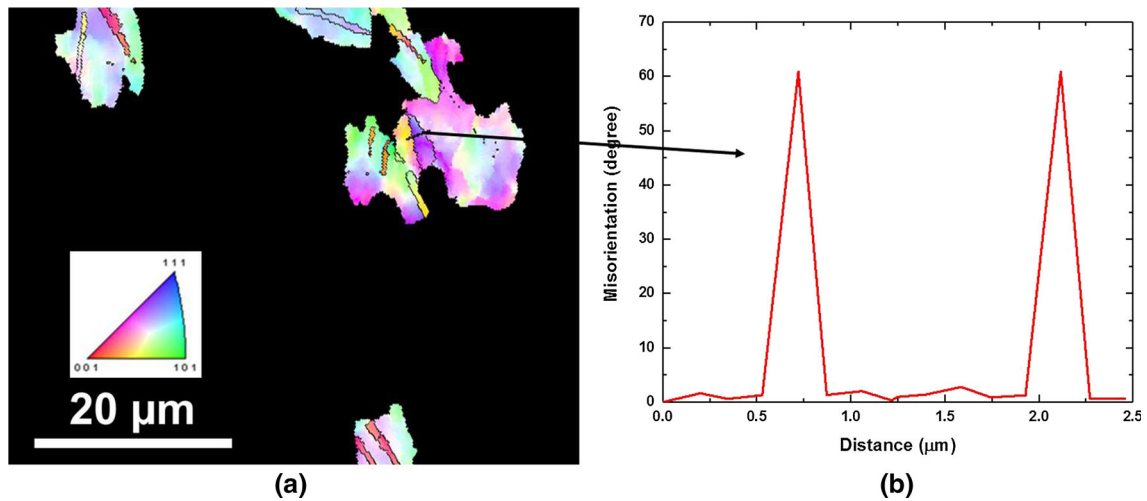


Fig. 8—(a) IPF map regions showing grains with twinning and (b) misorientation angle confirming twin boundaries in Ni-Si HEA D-pass-deformed specimen.

IV. DISCUSSION

A. Alloy Chemistry-Driven Phase Evolution in the As-cast and As-FSP HEAs

The chemistry of the two HEAs in the present study was selected based on the objective of tailoring the stability of γ (f.c.c.) for invoking transformation and twinning during deformation along with dislocation dominant plasticity. The existing literature on TRIP steels^[19–24] and HEAs^[25–30] suggests that f.c.c. lattice stability can be tuned by varying stacking fault energy to stabilize the single phase in the microstructure. However, recent study on design of metastable nonequiatomic HEAs opened a new pathway for in-building the various deformation modes in the material by providing metastability to γ (f.c.c.) phase.^[1–6] The greater the metastability of the γ (f.c.c.) phase, the more likely is the driving force for $\gamma \rightarrow \varepsilon$ transformation to occur, and a resultant enhanced plasticity.

The phase diagrams obtained from Thermocalc software for Ni-Si HEA and Co-Si HEA (Figures 9(a) and (b)) show clearly that Ni-Si HEA has a larger γ (f.c.c.) stabilized part at room temperature in the phase diagram compared with Co-Si HEA. The γ (f.c.c.)- ε (h.c.p.) two-phase region extended up to a higher temperature indicated higher metastability of γ (f.c.c.) phase in Co-Si HEA. This is attributed to the presence of Si, which increases the metastability of γ (f.c.c.) as explained earlier by Nene *et al.*^[12] However, in Ni-Si HEA, the influence of Ni toward increasing the γ (f.c.c.) phase stability is dominant over the effect of Si. Accordingly, the $\gamma \rightarrow \varepsilon$ transformation is more favorable in Co-Si HEA compared with Ni-Si HEA. Phase stability in the as-cast material was also confirmed by XRD (Figure 9(c)). The as-cast Ni-Si HEA only displayed peaks for the γ (f.c.c.) phase indicating the presence of a single-phase microstructure, whereas the as-cast Co-Si HEA specimen shows peaks for both γ

(f.c.c.) and ε (h.c.p.) phases. Therefore, clearly, just changing Ni to Co in the alloy chemistry results in substantial change in the γ (f.c.c.) lattice stability, and thus gives rise to different XRD spectra.

FSP imposes very high levels of strain and temperatures concurrently on the material.^[10] The increased γ metastability makes the phase stability sensitive to strain, strain rate, and temperature imposed during FSP. Higher temperature thermodynamically favors the stabilization of γ phase but the kinetics of transformation at high temperature is also dependent on the strain rate wherein the ε phase is favored at higher strain rate.^[13] The competition between temperature and deformation leads to responsive phase evolution during FSP and subsequent cooling from the processing temperature. As a result, Co-Si HEA being more metastable, showed higher ε (h.c.p.) fraction in D-pass specimen; while Ni-Si HEA retained single-phase γ (f.c.c.), as illustrated in Figure 9(d). Higher metastability of γ (f.c.c.) phase in Co-Si HEA than Ni-Si HEA is expected to result in a more favorable microstructure for invoking transformation-driven plasticity in the Co-Si HEA and twinning assisted deformation in the Ni-Si HEA.^[23]

B. Microstructure Dependence of the Mechanical Response

Microstructural evaluation of Ni-Si HEA after tensile test showed no change in the fraction of γ (f.c.c.) phase. This lack of active transformation is also confirmed by the absence of any ε (h.c.p.) peaks in the XRD pattern of Ni-Si HEA D-pass-deformed specimen (Figure 10(a)). On the other hand, as illustrated in Figure 10(b), Co-Si HEA showed $\gamma \rightarrow \varepsilon$ transformation after FSP. Moreover, this ε (h.c.p.) dominant dual-phase microstructure in D-pass condition with almost 15 pct change in the fraction of ε (h.c.p.) martensite after tensile deformation (Figure 10(b)) confirms the controlled involvement of

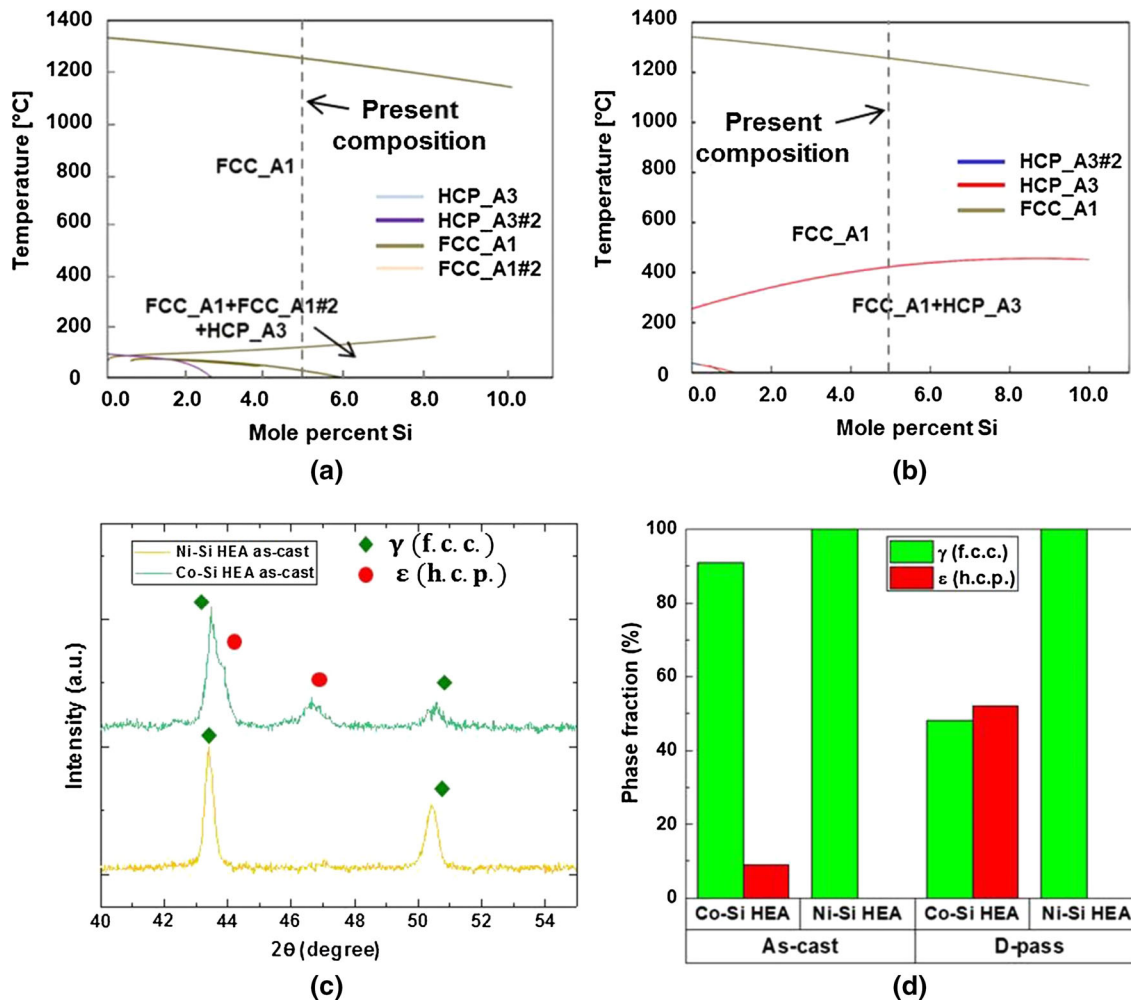


Fig. 9—(a-b) Phase diagrams obtained from Thermocalc of (a) Ni-Si HEA and (b) Co-Si HEA. (c) XRD patterns of the as-cast Ni-Si HEA and Co-Si HEA specimens. (d) Phase fractions from EBSD of γ (f.c.c.) and ϵ (h.c.p.) for the as-cast and D-pass FSP material for Ni-Si HEA and Co-Si HEA.

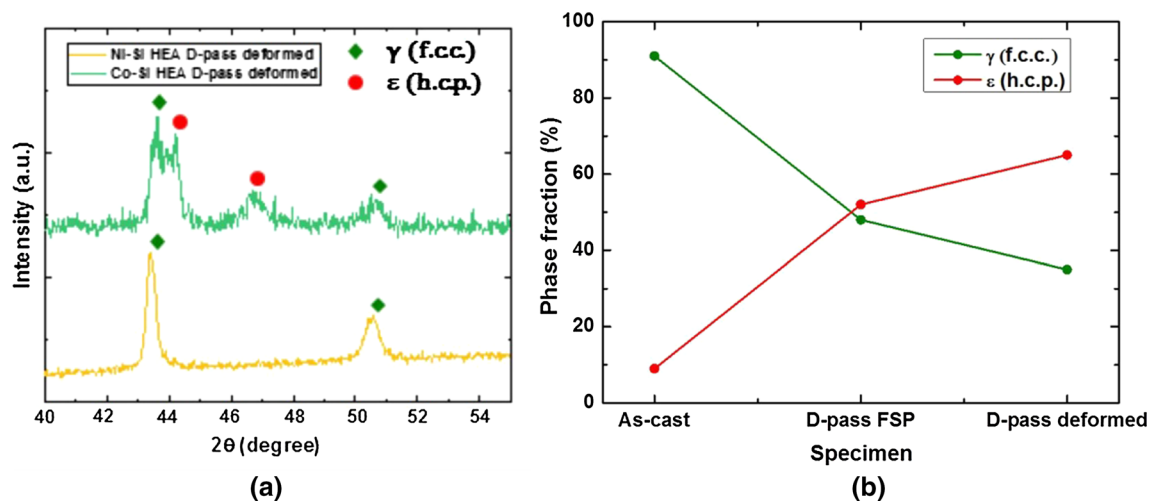


Fig. 10—(a) XRD patterns of D-pass-deformed specimens of Ni-Si HEA and Co-Si HEA and (b) fraction of γ (f.c.c.) and ϵ (h.c.p.) phases in the as-cast, D-pass FSP, and D-pass-deformed specimens of Co-Si HEA.

TRIP in Co-Si HEA. However, higher prior fraction of hard ε (h.c.p.) phase along with fine grain size imposes higher back stresses on the γ (f.c.c.) phase, thereby suppressing the $\gamma \rightarrow \varepsilon$ transformation during deformation. Therefore, the ε (h.c.p.) fraction in Co-Si HEA does not increase drastically from the as-FSP condition to the D-pass-deformed condition. Higher prior fraction of harder ε (h.c.p.) phase after D-pass FSP also triggered higher YS in Co-Si HEA than in Ni-Si HEA.^[12,13] Further, Co-Si HEA shows sustained work hardening over larger plastic strain regime than Ni-Si HEA (Figure 4(b)), irrespective of the same FSP condition. The sustainability of work hardening in dual-phase microstructures is attributed to uniform strain partitioning between the two phases during deformation. The sustained work hardening of Co-Si HEA suggests that, unlike single-phase Ni-Si HEA specimen, dual-phase Co-Si HEA specimen should have undergone sustained work hardening owing to the active participation of both ε (h.c.p.) and γ (f.c.c.) phases during deformation.

The higher stress accommodation at similar strain in Co-Si HEA is possible through the formation of ε (h.c.p.) martensite, or TRIP.^[31] Stress accommodation in a significant fraction of ε (h.c.p.) martensite phase leads to higher accommodation of dislocations in the dual-phase microstructure. Therefore, Co-Si HEA uses more effective grain refinement and transformation-induced dual-phase strain partitioning mechanisms to produce higher work hardening—wherein the ε (h.c.p.) phase uses the synergistic effect of various operative mechanisms like $\langle c + a \rangle$ dislocation-based mechanisms and also some deformation twinning to redistribute strain from the γ (f.c.c.) phase. On the other hand, limited twinning-induced plastic deformation of the γ (f.c.c.) phase incorporating insufficient strain-hardening ability in the relatively coarse-grained Ni-Si HEA leads to the inferior mechanical response in the latter.

V. CONCLUSIONS

The present comparative study of friction stir processed Ni-Si HEA and Co-Si HEA confirms that tailoring the alloy chemistry suitably to tune the microstructural and deformation mechanisms can substantially alter the tensile response. Specifically

- (1) The addition of Ni or Co substantially altered the phase evolution of Fe-Mn-Cr-Si-containing HEAs, and led to a single-phase microstructure in Ni-containing HEA (Ni-Si HEA), but dual-phase microstructure in Co-containing HEA (Co-Si HEA) in the as-cast condition.
- (2) FSP with two overlapping passes on Ni-Si HEA resulted in grain-refined γ (f.c.c.) microstructure as against the ε (h.c.p.)-dominant dual-phase microstructure in Co-Si HEA. This variation in microstructural evolution is a strong indication of higher γ phase metastability in Co-Si HEA than Ni-Si HEA.
- (3) Co-Si HEA possesses higher work-hardening capability due to controlled γ (f.c.c.) to ε (h.c.p.)

transformation and uniform strain partitioning in the γ (f.c.c.) and ε (h.c.p.) phases compared with Ni-Si HEA, which is coarse-grained and has limited twinning-mediated strain-hardening ability. As a result, Co-Si HEA allows higher dislocation accommodation at similar strains than Ni-Si HEA, leading to higher strength without loss in ductility in the former.

ACKNOWLEDGMENTS

The current study was performed under a Cooperative Agreement between the Army Research Laboratory and the University of North Texas (W911NF-13-2-0018). The authors thank the Center for Advanced Research and Technology for allowing access to microscopy facilities at the University of North Texas. The authors also acknowledge the help of J. Reeder, S. Zellner, and L. Reza Nieto in EBSD and tensile specimen preparation.

REFERENCES

1. Y. Deng, C.C. Tasan, K.G. Pradeep, H. Springer, A. Kostka, and D. Raabe: *Acta Mater.*, 2015, vol. 94, pp. 124–33.
2. Z. Li, K.G. Pradeep, Y. Deng, D. Raabe, and C.C. Tasan: *Nature*, 2016, vol. 534, pp. 227–30.
3. Z. Li and D. Raabe: *JOM*, 2017, vol. 69, pp. 2099–2106.
4. Z. Li, C.C. Tasan, H. Springer, B. Gault, and D. Raabe: *Sci. Rep.*, 2017, vol. 7, pp. 40704-1–04-7.
5. Z. Li, C.C. Tasan, K.G. Pradeep, and D. Raabe: *Acta Mater.*, 2017, vol. 131, pp. 323–35.
6. M. Wang, Z. Li, and D. Raabe: *Acta Mater.*, 2018, vol. 147, pp. 236–46.
7. J.-W. Yeh: *Ann. Chim. Sci. Mater.*, 2006, vol. 31, pp. 633–48.
8. M.C. Gao, J.-W. Yeh, P.K. Liaw, and Y. Zhang: *High-Entropy Alloys Fundamentals and Applications*, Springer, Cham, 2016, pp. 53–64.
9. D.B. Miracle and O.N. Senkov: *Acta Mater.*, 2017, vol. 122, pp. 448–511.
10. S. Palanivel, A. Arora, K.J. Doherty, and R.S. Mishra: *Mater. Sci. Eng. A*, 2016, vol. 678, pp. 308–14.
11. S.S. Nene, K. Liu, M. Frank, R.S. Mishra, R.E. Brennan, K.C. Cho, Z. Li, and D. Raabe: *Sci. Rep.*, 2017, vol. 7, pp. 16167-1–67-7.
12. S.S. Nene, M. Frank, K. Liu, R.S. Mishra, B.A. McWilliams, and K.C. Cho: *Sci. Rep.*, 2018, vol. 8, pp. 9920-1–20-1.
13. S.S. Nene, M. Frank, K. Liu, S. Sinha, R.S. Mishra, B. McWilliams, and K.C. Cho: *Scripta Mater.*, 2018, vol. 154, pp. 163–67.
14. D.B. Miracle, J.D. Miller, O.N. Senkov, C. Woodward, M.D. Uchic, and J. Tiley: *Entropy*, 2014, vol. 16, pp. 494–525.
15. S. Chikumba and V.V. Rao: *7th ICLTET Proc. High Entropy Alloys: Dev. Appl.*, 2015, pp. 13–17. http://ieng.org/images/proceedings_pdf/9705E1115005.pdf, accessed 19 Sep 2018.
16. D.P. Field, C.C. Merriman, and I.N. Mastorakos: *Solid State Phenom.*, 2010, vol. 160, pp. 17–22.
17. M.A. Meyers, O. Vohringer, and V.A. Lubarda: *Acta Mater.*, 2001, vol. 49, pp. 4025–39.
18. Y.T. Zhu, X.Z. Liao, X.L. Wu, and J. Narayan: *J. Mater. Sci.*, 2013, vol. 48, pp. 4467–75.
19. F. Trichter, A. Rabinkin, M. Ron, and A. Sharfstein: *Scripta Metall.*, 1978, vol. 12, pp. 431–34.
20. D.T. Pierce, J.A. Jiménez, J. Bentley, D. Raabe, C. Oskay, and J.E. Wittig: *Acta Mater.*, 2014, vol. 68, pp. 238–53.

21. S. Martin, C. Ullrich, and D. Rafaja: *Mater. Today Proc.*, 2015, vol. 2, pp. 643–46.
22. S. Martin, S. Wolf, U. Martin, L. Kruger, and D. Rafaja: *Metall. Mater. Trans. A*, 2016, vol. 47A, pp. 49–58.
23. E.I. Galindo-Nava and P.E.J. Rivera-Díaz-del-Castillo: *Acta Mater.*, 2017, vol. 128, pp. 120–34.
24. R. Xiong, H. Peng, H. Si, W. Zhang, and Y. Wen: *Mater. Sci. Eng. A*, 2014, vol. 598, pp. 376–86.
25. A.J. Zaddach, C. Niu, C.C. Koch, and D.L. Irving: *JOM*, 2013, vol. 65, pp. 1780–89.
26. E. Otto, A. Dlouhy, Ch. Somsen, H. Bei, G. Eggeler, and E.P. George: *Acta Mater.*, 2013, vol. 61, pp. 5743–55.
27. S. Huang, W. Lei, S. Lu, F. Tian, J. Shen, E. Holmstrom, and L. Vitos: *Scripta Mater.*, 2015, vol. 108, pp. 44–47.
28. A.J. Zaddach, R.O. Scattergood, and C.C. Koch: *Mater. Sci. Eng. A*, 2015, vol. 636, pp. 373–78.
29. N.L. Okamoto, S. Fujimoto, Y. Kambara, M. Kawamura, Z.M.T. Chen, H. Matsunoshita, K. Tanaka, H. Inui, and E.P. George: *Sci. Rep.*, 2016, vol. 6, pp. 35863-1–63-10.
30. S.F. Liu, Y. Wu, H.T. Wang, J.Y. He, J.B. Liu, C.X. Chen, X.J. Liu, H. Wang, and Z.P. Lu: *Intermetallics*, 2018, vol. 93, pp. 269–73.
31. G.B. Olson and M. Cohen: *Metall. Trans. A*, 1976, vol. 7A, pp. 1897–1904.